Available online at www.sciencedirect.com

ScienceDirect

Journal of Magnesium and Alloys 9 (2021) 569–580

www.elsevier.com/locate/jma

Effect of lithium content on the mechanical and corrosion behaviors of HCP binary Mg–Li alloys

Chuanqiang Li*, Yibin He, Huaipei Huang

School of Materials and Energy, Guangdong University of Technology, Guangzhou 510006, China

Received 4 December 2019; received in revised form 3 January 2020; accepted 13 February 2020
Available online 29 September 2020

Abstract

The microstructure, crystallographic texture, mechanical properties and corrosion resistance of as-extruded HCP Mg-xLi ($x=1$, 3, 5; in wt%) alloys were investigated. The results indicated that the HCP Mg-5Li alloy with high lithium content exhibited a low degree of dynamic recrystallization (DRX) compared with Mg-1Li and Mg-3Li alloys. Besides, the 45° base (0001) texture of Mg-1Li alloy could turn into (11–20) and (10–10) prismatic texture of Mg-3Li and Mg-5Li alloys with c-axis approximately parallel to transverse direction (TD). As a result, the strong prismatic texture resulted in the mechanical anisotropy of as-extruded Mg-3Li and Mg-5Li alloys with higher mechanical strength and low elongation along extrusion direction (ED) (reverse for TD sample). Regarding of corrosion behaviors, filiform corrosion occurred in the three Mg–Li alloys, whilst the high lithium content could mitigate the groove-like corrosion and improve the corrosion resistance of Mg-5Li alloy, which was ascribed to the refined grains, prismatic texture and surface film.

Keywords: Mg–Li alloys; Recrystallization; Texture; Mechanical properties; Corrosion behavior.

1. Introduction

Alloying Mg with the lightest metal element of Li (0.53 g/cm^3) could be further lightweight, allowing for an increase in plasticity [1–6]. The ultra-lightweight structured Mg–Li alloys presented significant promise in automotive, aerospace and electronics [5,6]. Compared with traditional hexagonal close-packed (HCP) Mg alloys, the Mg–Li system exhibited different crystal structure based on the lithium content, which was unique in comparison to other alloying addition to Mg. The stable room-temperature phase of Mg–Li alloy was: i) a hexagonal close-packed (HCP) α-Mg with less than 5.5 wt% Li; ii) a body centered cubic (BCC) β-Li with more than 10.3 wt% Li; and iii) a duplex (α-Mg + β-Li) structure between 5.5 wt% and 10.3 wt% Li [7,8]. However, the mechanical strength and corrosion resistance of Mg–Li alloys were generally inferior to the Mg alloys without lithium [9–13].

As for the strengthening strategies of metal materials, the mechanical processing (extrusion, rolling, forging, etc.) was the common approach to optimize microstructure with the fine gains and/or broken second phases [14–17]. Regarding of Mg alloys, the deforming Mg alloys always exhibited strong basal textures, making the c-axis of most grains nearly parallel to the normal direction (ND) of the sheet [18–20]. However, the lithium addition could weaken the basal texture of Mg alloys as the rotation of basal plane to the transverse direction would be promoted by the decreased c/a ratio of Mg–Li alloys [13,21–23]. Compared with AZ31 alloy, Mg-4Li alloy possessed weak basal (0002) and prismatic (10–10) texture at the same cold-rolling reduction [13]. Previous works reported that the addition of Li could restrained the ⟨a⟩ basal slip and promoted the ⟨a⟩ prismatic slip of hexagonal Mg–Li alloys [24–26]. For example, lower critical resolved shear stress (CRSS) in the ⟨a⟩ prismatic slip and higher in the ⟨a⟩ basal slip occurred in the Mg-4 wt% Li single crystals

* Corresponding author.
E-mail address: cqli13s@alum.imr.ac.cn (C. Li).

https://doi.org/10.1016/j.jma.2020.02.022

[24]. Agnew et al. demonstrated that the $\langle c+a \rangle$ pyramidal slip in Mg alloys could be activated by the adding lithium [25]. At the same time, the increase of $\langle c+a \rangle$ pyramidal slip could lead to the enhanced ductility of Mg alloys, which was proved by the viscoplastic self-consistent simulations [25]. To confirm the former studies, abundant uniformly distributed $\langle c+a \rangle$ dislocations of deformed Mg–Li alloys were found by transmission electron microscopy (TEM) [26]. Compared with a conventional magnesium AZ31 alloy, Al-Samman reported that lithium addition to magnesium (Mg-4 wt% Li) exhibited remarkable room temperature ductility improvement owing to enhanced activity of non-basal slip, particularly, $<c+a>$-slip mode [13]. Many reports had focused on the texture evolution of α-Mg phase in Mg–Li alloys, and the results showed that the addition of Li weakened (0001) basal texture and increased the deflection of basal planes along normal direction to rolling direction or transverse direction, which was associated with the activation of non-basal slip systems and the formation of DRX grains [21,27–29]. Recently, Li and Xu revealed the different effect of quasicrystal phases on the crystal texture and mechanical of three typical Mg–Li alloys (HCP, HCP+BCC and BCC) [30–32]. However, so far, few reports could be referred to clarify the effect of lithium concentration on the texture and/or mechanical behaviors on the single Mg–Li system (HCP, HCP+BCC or BCC).

Compared with massive reports on the mechanical properties of Mg–Li alloys, the research on the corrosion behaviors of strengthening Mg–Li alloy was deficient to date. It was well known that lithium was much more electrochemical/chemical active than magnesium, the addition of Li into multicomponent Mg matrix could further deteriorate the integrity of Mg matrix in aqueous solution and caused a worse corrosion resistance than conventional Mg alloys [33–35]. To improve the corrosion resistance of Mg–Li alloys, regulating the matrix microstructure (alloying, second phases, deformation, heat treatment) and surface modification were the common methods [36–40]. For example, the formation of I-phase by alloying with a certain Zn/RE ratio could effectively retard the corrosion proceeding of as-cast Mg-6Li alloy and the corrosion resistance of Mg-8.8Li alloy was improved remarkably by the phosphate conversion film [36,37]. Recently, high-corrosion-resistant Mg alloy was reported in Mg–Li system, which was ascribed to the protective and self-healing Li_2CO_3 film deposited on the surface [41–46]. Li et al. reported that corrosion resistance of binary BCC Mg-14Li alloy was enhanced with immersion time in 0.1 M NaCl solution and always higher than those of HCP Mg-4Li and HCP+BCC Mg-7.5Li alloys [43]. Following this hypothesis, the corrosion behaviors or surface film of Mg–Li alloys should be correlated closely with lithium concentration, implying the possible difference of corrosion resistance for HCP Mg–Li alloys with different lithium content. On the other hand, it seems that the effect of lithium concentration on the mechanical and corrosion performance of Mg–Li alloys can not be covered for all the Mg–Li system as their crystallographic structure would be altered with lithium content. As a result, it was necessary and significant to separate the HCP, HCP+BCC and BCC Mg–Li alloys and elucidated the concrete effect of lithium content on the mechanical and corrosion behaviors for each Mg–Li system.

Table 1
Chemical composition of Mg–Li alloys in experiment.

Alloy	Chemical composition (in wt.%)	
	Mg	Li
Mg-1Li	Bal.	1.06
Mg-3Li	Bal.	2.99
Mg-5Li	Bal.	4.97

Based on the aforementioned descriptions and analysis, to deepen the fundamental understanding on the mechanical and corrosion behaviors of Mg–Li alloys, binary HCP Mg–Li alloys was used herein to isolate the effects of additional alloying elements and crystallographic structure. Moreover, the underneath failure mechanisms of tension and corrosion for HCP Mg–Li alloys with different lithium content would be characterized and compared in detail.

2. Material and methods

2.1. Materials and microstructural analysis

The initial materials used herein were as-extruded Mg-1Li, Mg-3Li and Mg-5Li (in wt.%) alloys plates whose chemical composition was determined by inductively coupled plasma atomic emission spectrum (ICP-AES) apparatus and the results were shown in Table 1. After casting, the ingots were homogenized at 400 °C for 6 h with the protection of several layers of wrapped Al foil. Then, the ingots were extruded into thick plate with cross section of 12 mm × 50 mm at 300 °C, with an extrusion ratio of about 6.5. Sample pieces cut from the extruded plates were ground with SiC papers up to 5000 grit finish and then finely polished up to a 1 μm finish with ethanol.

Microstructure of the alloys were observed by optical microscopy (OM), scanning electron microscopy (SEM; JEOL JSM-IT100) and electron back-scattering diffraction (EBSD). To reveal the difference of grain structure between the alloys, polished samples were etched with 5% nitric acid + 95% ethanol. Average grain size was determined by using the mean linear intercept method. Distributed intensity of the (0002), (11–20) and (10–10) pole figures for the three alloys were measured by EBSD analysis. For EBSD tests, one surface of the sample was mechanically polished and followed by electropolishing in a commercial electrolyte (AC2). EBSD analyses were conducted on a scanning electron microscope (SEM, FEI NOVA400 SEM with Oxford-EBSD system) using a step size of 2 μm. All EBSD measurement were conducted from a normal plane of as-extruded plate and all EBSD data were analyzed using the Channel 5 software.

2.2. Mechanical testing

Tensile samples with a gauge length of 20 mm, width of 3 mm and thickness of 3 mm were machined from the

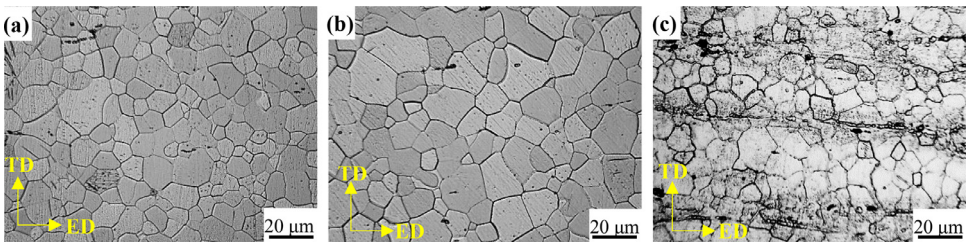

Fig. 1. Optical observations to the etched (a) Mg-1Li, (b) Mg-3Li and (c) Mg-5Li samples.

as-extruded plates. Moreover, samples with axial direction parallel to the transverse and extrusion directions of the plates were defined as "TD" and "ED" samples, respectively. Tensile tests were conducted on a SHIMADZU (Servo, 5 KN) testing machine at a constant strain rate of 1×10^{-3} s^{-1} at room temperature and all measurements were repeated at least three times. For tensile samples, one side of the gauge section were finely polished before testing. Afterwards, the wide surface near fractures and fracture surfaces was observed by SEM with the modes of secondary electron (SE).

2.3. Corrosion testing

2.3.1. Immersion and mass loss testing

To study corrosion performance, the Mg–Li alloys samples with dimensions of 12 mm × 10 mm × 3 mm were immersed in 0.1 M neutral NaCl solution (pH = 6.9) for a certain time at room temperature. After immersion, samples were cleaned to remove corrosion products from surface using a chromic acid consisting of 180 g/L CrO_3 [47]. Afterwards, surface morphology of the cleaned samples was observed by OM, confocal laser scanning microscopy (CLSM, OLYMPUS LEXT OLS4000) and SEM. Regarding of mass loss testing, the samples were immersed in 0.1 M NaCl solution at room temperature for 3 days. Following the exposure period, a cleaning solution was used to remove corrosion products and then calculated the mass loss rates. Three replicates were carried out for each condition to ensure the reproducibility. Surface chemistry of specimens subjected to 2 h immersion in 0.1 M NaCl was analyzed by X-ray photoelectron spectroscopy (XPS, Escalab 250Xi, Thermo Fisher). The measured binding energy values were calibrated by the C1s (hydrocarbon C–C, C–H) of 285 eV.

2.3.2. Electrochemical analysis

Potentiodynamic polarization measurements were carried out with a scan rate of 1 mV/s by using a Wuhan CorrTest electrochemistry test system (CS350H). A classical three-electrode cell was used with platinum as counter electrode, saturated calomel electrode (SCE) as reference electrode and the samples with an exposed area of 1 cm^2 as working electrode. The measurements were performed in 0.1 M NaCl solution at room temperature. The scan frequency of electrochemical impedance spectroscopy (EIS) was executed over a frequency range from 100 kHz to 10 mHz with 10 mV of amplitude of sinusoidal potential signals with respect to the open circuit potential (OCP). To ensure the reliability, at least three replicates were carried out for each test and initial delay of 600 s was set for polarization and EIS measurements to ensure a relative stabilized testing system at OCP [48].

3. Results

3.1. Microstructure and texture analysis

The microstructure of as-extruded Mg-1Li, Mg-3Li and Mg-5Li alloys are shown in Fig. 1, indicating that the deforming characteristics of the microstructure is trivial (especially for Mg-1Li and Mg-3Li alloys) and equiaxial grain structure forms in the three alloys. On the other hand, the grain size is not uniform for the three alloys with larger grains (>20 μm) and smaller ones (<5 μm). The average grain size of Mg-1Li, Mg-3Li and Mg-5Li alloys are 23.1 μm, 24.8 μm and 17.5 μm, respectively. The results illustrates that the grain size of HCP Mg–Li alloy grows up slightly and then decreases with the increasing lithium content.

The presence of equiaxial grains of the three as-extruded alloys demonstrates the occurrence of recrystallization during hot extrusion. To further confirm the volume fraction of recrystallized, substructured and deformed grains, EBSD analysis was conducted, as shown in Fig. 2. The blue, yellow and red regions represent the recrystallized, substructured and deformation grains, respectively. It can be seen that the Mg-1Li and Mg-3Li alloys present the approximative percentage of each typed grain. However, the counterparts of Mg-5Li alloy change apparently, *i.e.* the volume fraction of recrystallized grains decrease from ~96% of Mg-1Li and Mg-3Li alloys to ~86% of Mg-5Li alloy; the substructured grains increase from 2~3% of Mg-1Li and Mg-3Li alloys to ~7% of Mg-5Li alloy; the deformed grains increase from ~1% of Mg-1Li and Mg-3Li alloys to ~6.5% of Mg-5Li alloy. Based on the above analysis, almost completed recrystallization occurs in both Mg-1Li and Mg-3Li alloys, whilst the Mg-5Li alloy possess more substructured and deformed grains. Therefore, it can be deduced that the increasing lithium concentration can restrain the occurrence of recrystallization for HCP Mg–Li alloy.

The grain orientation of Mg alloys would be altered after deformation and the strong base texture was a general character, whilst the addition of lithium could change the texture of traditional magnesium alloys [28,29]. In this work, the oriented grain distribution of Mg-1Li, Mg-3Li and

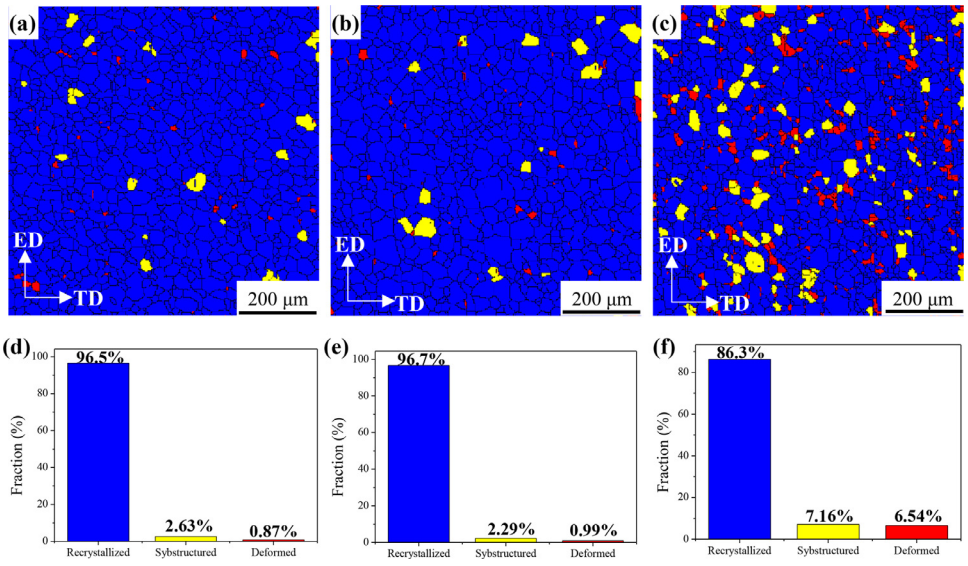

Fig. 2. Recrystallized (a-c) maps and (d-f) histograms of as-extruded (a) (d) Mg-1Li, (b) (e) Mg-3Li and (c) (f) Mg-5Li alloys analyzed by EBSD.

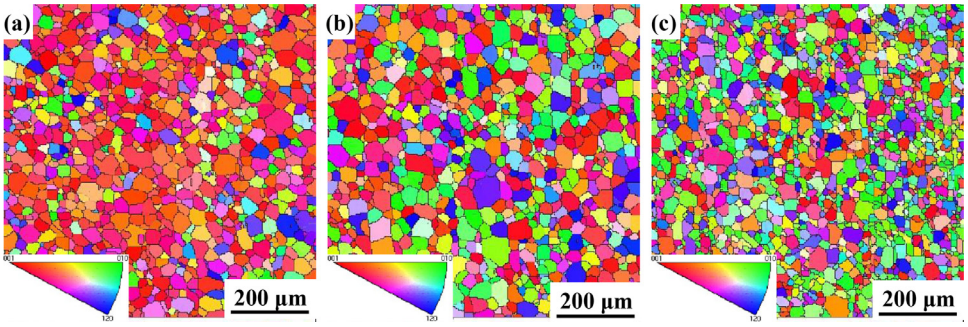

Fig. 3. Orientation maps of as-extruded (a) Mg-1Li, (b) Mg-3Li and (c) Mg-5Li alloys analyzed by EBSD.

Mg-5Li alloys are shown in Fig. 3, where the different colors indicate different crystallographic orientations of the grains. It should be noted that the near red grains decrease with the increasing lithium concentration, whilst it is reversed for the green and blue grains. Namely, the near base (0001) texture gradually transforms into the prismatic (11–20) and (10–10) texture with the increasing lithium in HCP Mg–Li alloy. In addition, the grain size of Mg-5Li alloy is refined, whilst the counterparts of Mg-1Li and Mg-3Li alloys are similar and larger than that of Mg-5Li alloy, which is corresponding to the OM results (Fig. 1).

To further clarify the texture of the three alloys, the (0001), (11–20) and (10–10) pole figures are shown in Fig. 4. It can be seen that the base (0001) texture of Mg-1Li alloy is weaker than that of non-lithium Mg alloys, *i.e.* the c-axis of Mg-1Li alloy deviated 45° from ND (normal direction) and presents 45° with respect to ED (extrusion direction) and TD (transversal direction) simultaneously in the projective ED × TD plane, which can be defined as 45° base texture herein. Meanwhile, the (11–20) and (10–10) prismatic texture are scattered. When the lithium content increases up to 3 wt%, the c-axis of Mg-3Li alloy tilts about 60° away ND and exhibits about 10° toward TD (80° away ED). In addition, the (10–10) prismatic texture emerges, *i.e.* the (10–10) plane is approximately vertical to the ED. Regarding of Mg-5Li alloy, the c-axis further tilts about 85° away ED (almost paralleling to TD). Besides, the (10–10) prismatic texture is also apparent. Furtherly, based on the texture intensity and grain orientation distribution, the base (0001) texture become weaker and the prismatic (10–10) and (11–20) texture enhance obviously with the increasing lithium content in HCP Mg–Li system. Therefore, the increasing lithium content can alter the crystallographic texture from the 45° (0001) base texture of Mg-1Li alloy to (10–10) and (11–20) prismatic texture of Mg-5Li alloy effectively.

3.2. Mechanical behaviors and fracture analysis

Fig. 5 shows the stress-stain tensile curves evaluated along ED and TD of as-extruded Mg-*x*Li ($x = 1$, 3, 5, wt%) alloys. It can be seen that the Mg-1Li alloy shows the mechanical isotropy along both ED and TD, whilst the mechanical anisotropy occurs for Mg-3Li alloy. Namely, ED sample of Mg-3Li alloy presents high mechanical strength and low elongation, whilst it is reversed for TD sample. When the lithium content increases up to 5 wt%, the similar mechanical anisotropy of Mg-5Li alloy still exists. Additionally, it should be noted that the stress-strain curves of Mg-5Li alloy show serrated characterization when the tension is conducted

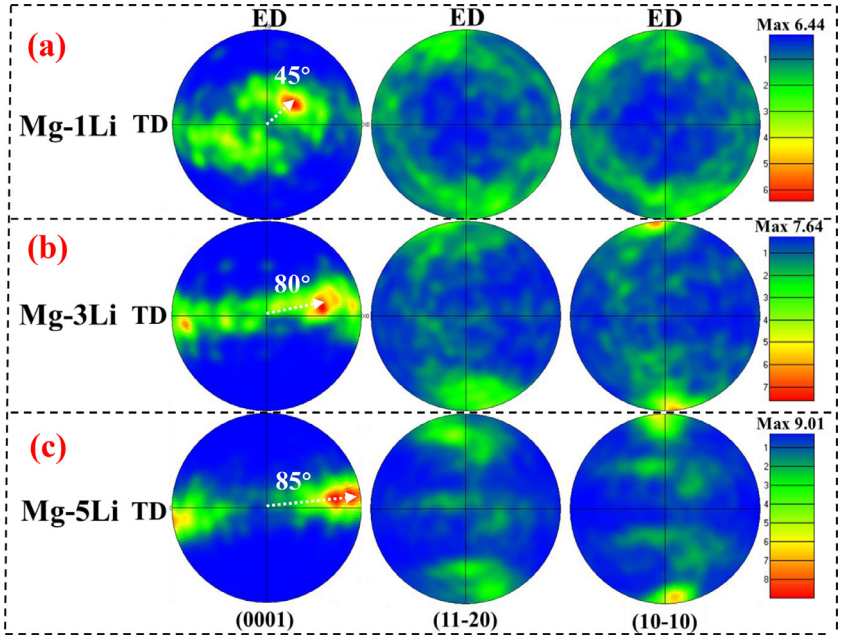

Fig. 4. Pole figures of as-extruded (a) Mg-1Li, (b) Mg-3Li and (c) Mg-5Li alloys analyzed by EBSD.

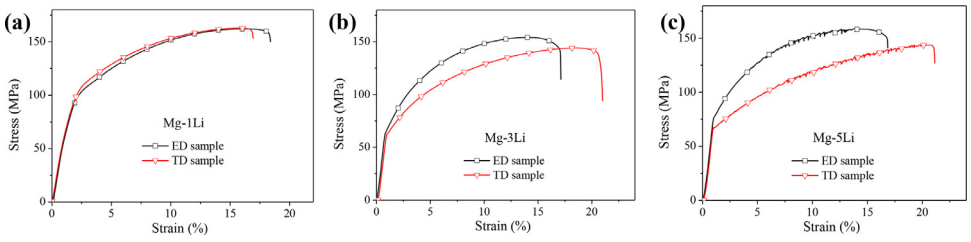

Fig. 5. Engineering stress-strain curves of as-extruded (a) Mg-1Li, (b) Mg-3Li and (c) Mg-5Li alloys along the extrusion direction (ED) and transverse direction (TD).

along both ED and TD direction (Fig. 5c), which is defined as Portevin-Le Chatelier effect. In general, the main mechanism of PLC effect could be ascribed to the dynamic strain aging (DSA), *i.e.* the repeated pinning and unpinning process of dislocations at solute atoms occurs when the diffusion velocity of solute atoms was compared to the moving rate of mobile dislocations in magnitude [49–52]. On the other hand, some other possible mechanisms had also been proposed to account for the PLC effect, such as extensive twins, shearing of precipitates by dislocations [51,52]. It should be notable that no precipitations are formed in the binary Mg-5Li alloy (Fig. 1) and deformation twins are also hardly observed on the fracture side surface (shown in Fig. 6 described as following). As a result, the PLC effect occurring in Mg-5Li alloy can be ascribed to the DSA. In terms of Mg-1Li and Mg-3Li alloys with less lithium concentration, the diffusion velocity of solute atoms should be lower than that the moving rate of mobile dislocations at this temperature, resulting in smooth stress-strain curves. Therefore, the PLC effect (serrated flow) of Mg–Li alloy is closely related to the lithium content and the critical value needs to be confirmed in the future work.

To describe and compare the measured data, the mechanical properties of 0.2% proof yield strength (YS), ultimate tensile strength (UTS) and elongation ratio to failure (EL) of the three alloys are listed in Table 2. Compared with the YS (93 MPa/97 MPa of ED/TD sample) and UTS (162 MPa/163 MPa of ED/TD sample) of Mg-1Li alloy, the YS (65 MPa/61 MPa of ED/TD sample) and UTS (154 MPa/144 MPa of ED/TD sample) of Mg-3Li alloy are slightly low, whereas the EL is inverse. Moreover, the mechanical strength of Mg-5Li alloy presents an elevation when compared with Mg-3Li alloy, which is ascribed to the refinement strengthening and/or solution strengthening of lithium. As a result, the effect of lithium on the mechanical performance of HCP Mg–Li alloy is dependent on the lithium

Table 2
Tensile properties of as-extruded three Mg–Li alloys along ED and TD orientations.

Alloy	Orientation	YS (MPa)	UTS (MPa)	EL (%)
Mg-1Li	ED	93±5	162±7	15±2
	TD	97±6	163±5	14±2
Mg-3Li	ED	65±4	154±6	16±3
	TD	61±5	144±6	19±2
Mg-5Li	ED	77±5	159±4	17±4
	TD	66±6	144±5	19±3

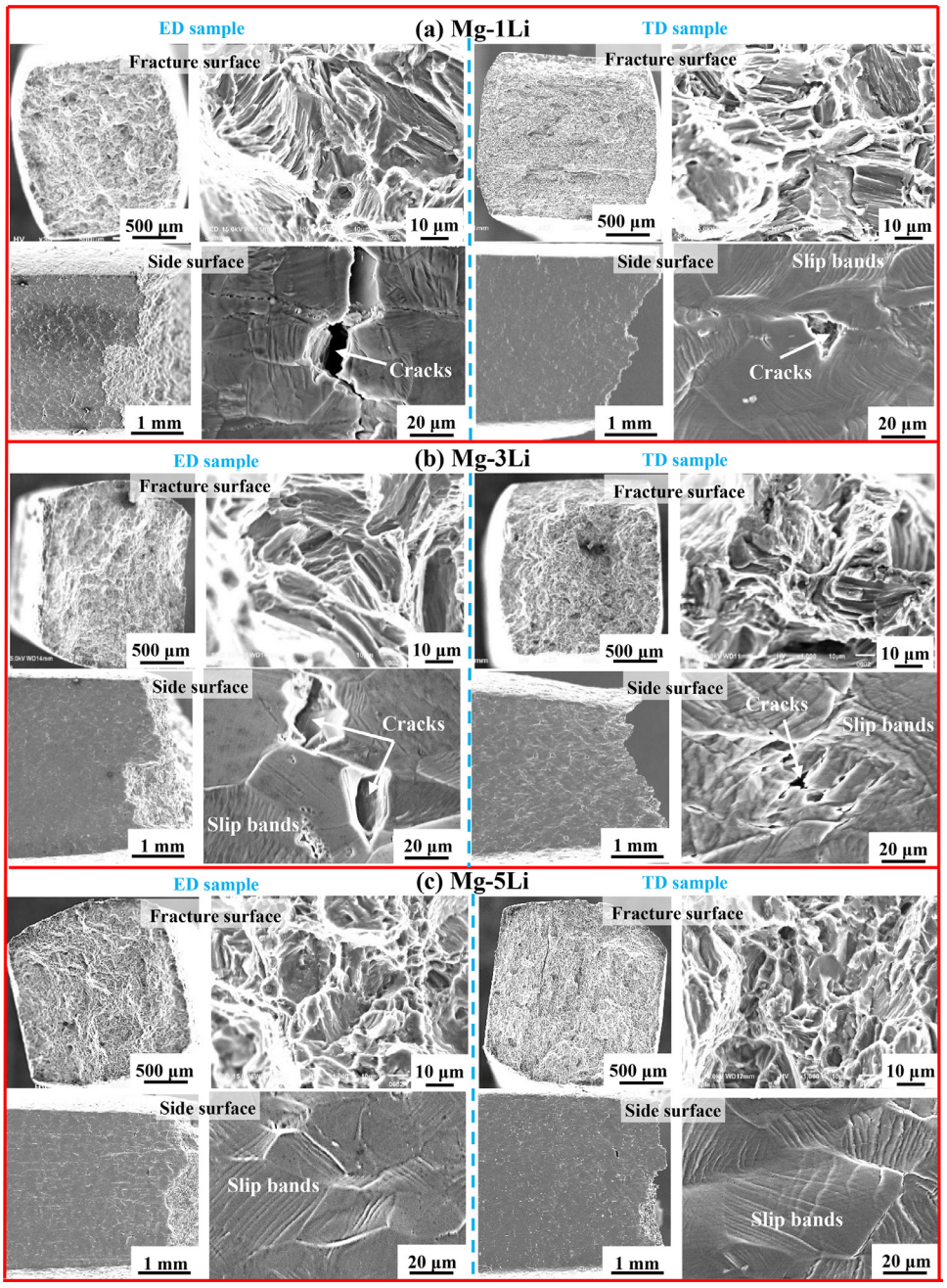

Fig. 6. SEM Observations to the fracture surfaces and side surfaces of (a) Mg-1Li, (b) Mg-3Li and (c) Mg-5Li alloys.

concentration, which is also in consistent with the previous work [21].

To reflect and compare the deformed microstructures of the three HCP Mg–Li alloys along differently orientations, the fracture surfaces and morphologies of side surfaces within a distance of about 1 mm from the fracture sites are observed, as shown in Fig. 6. For the Mg-1Li alloy, the fracture surfaces of both ED and TD samples are quite similar and mainly composed of tearing ridge and cleavage plane, which is a typical mixed ductile-brittle fracture. The side morphologies reveal that the surface is flat and no necking occurs in the low-magnified observation, whilst the obvious deformation bands and micro-cracks can be observed in the high magnification for both ED and TD samples. Meanwhile, micro-cracks initiate and propagate preferentially along the deformed bands, which is corresponding to the tearing ridge and/or plane in the fracture surface. In terms of Mg-3Li alloy, the fracture surface of ED and TD samples present a little difference, the tearing ridge of ED sample gradually transforms into tearing dimple of TD sample. Generally, plastic dimples can accommodate plastic strain during the tensile testing. As a result, the plasticity of TD sample is better than that of ED sample, which is in consistent with the tensile curves shown in Fig. 5b. The side fracture morphologies of Mg-3Li alloy show that the

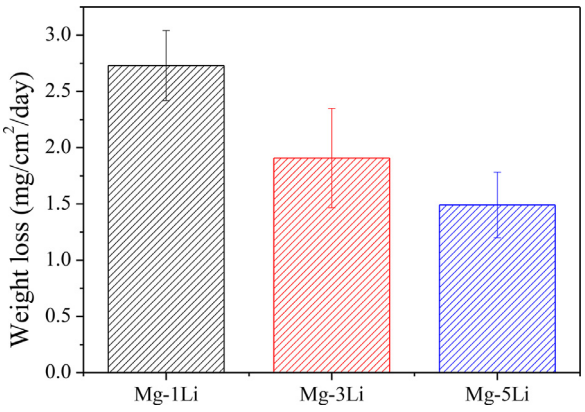

Fig. 7. Weight loss of Mg-1Li, Mg-3Li and Mg-5Li alloys exposed to 0.1 M NaCl for 3 days.

necking occurs in TD sample and the deformation characterization with high density of slip bands and more micro-cracks is conspicuous. Therefore, all the deformation evidences prove a better deforming capacity when the tension of as-extruded Mg-3Li alloys is conducted along TD direction. Additionally, the side fracture morphology of ED sample is flat and only sparse slips can be observed, concomitant with a lower EL value. As for Mg-5Li alloy, the ductile fracture of ED and TD samples is obvious since a lot of dimples occur on the fracture surface. Compared with ED sample, the TD sample possess much more and deeper dimples, corresponding to a better plasticity shown in Fig. 5c. Besides, more dense slip bands with some cross-slips occurs in TD sample of Mg-5Li alloy compared with the ED sample, which further elucidates higher EL of TD sample. Moreover, the size of micro-cracks initiated at slip bands of Mg-5Li alloy decreases compared with the side fracture morphologies of Mg-1Li and Mg-3Li alloys, implying a relative uniform deformation occurred in HCP Mg–Li alloy with high lithium content.

3.3. Corrosion behaviors

The immersion testing is a practicable way to evaluate the corrosion prosperity of magnesium alloy by calculating the weight loss ratio, and the achieved weight loss rate of the Mg-1Li, Mg-3Li and Mg-5Li alloys are shown in Fig. 7. In general, the mass loss results represent corrosion rate directly and the average mass loss rate determined for Mg-1Li, Mg-3Li and Mg-5Li immersed in 0.1 M NaCl for 3 days are 2.7, 1.9 and 1.5 mg/cm^2/day, respectively. Namely, the mass loss rate of Mg-5Li alloy is less than those of Mg-1Li and Mg-3Li alloys, indicating that the high Li content is capable of reducing the corrosion rate in the HCP Mg–Li system.

The surface morphologies of Mg-1Li, Mg-3Li and Mg-5Li alloys immersed in 0.1 M NaCl for 16 h are shown to rely strongly on the Li content, as shown in Fig. 8. The corrosion of Mg-1Li alloy reveals a deep groove-like corrosion morphology propagating along the ED direction preferentially. Such a groove-like corrosion morphology is associated with the reported scenario whereby local anode and cathode sites dynamically evolve [53–55]. With the lithium content increasing up to 3 wt.%, the groove-like corrosion morphology of Mg-3Li alloy becomes weaker. Compared with Mg-1Li and Mg-3Li alloys, the corrosion of Mg-5Li alloy is superficial and no obvious groove-like corrosion morphology is observed, consistent with the results of mass loss measurements. Besides, it is noted that the other areas on the surface of the Mg–Li alloys following 16 h immersion appears to be also corroded apart from the apparent groove-like morphology, and therefore it is deemed essential to carry out SEM observation.

The SEM observations to the corroded surfaces of three Mg–Li alloys after immersion in 0.1 M NaCl for 2 h are shown in Fig. 9, clarifying the microstructure dependent corrosion behavior. It should be notable that all the three HCP Mg–Li alloys show the typical feature of filiform corrosion in the lower magnification. Besides, the corrosion 'filaments' with different orientations in different areas of the sample surface are seen in the high-magnified observation, which is associated with the anisotropy of different grains where the corrosion is occurring. On the other hand, larger and deeper corrosion pits also occur in Mg-1Li alloys and the corrosion filaments (Fig. 9d) are destroyed, corresponding to the worst corrosion resistance amongst the three Mg–Li alloys. The number of corrosion pits with smaller size occurring in Mg-3Li alloy decrease and the corrosion filaments are prominent but slender, implying a better corrosion resistance than that of Mg-1Li alloy. With the lithium content increasing, the Mg-5Li alloy shows no corrosion pits on its surface after 2 h immersion and the apparent corrosion filaments are much finer than that of Mg-3Li alloy (Fig. 9f), indicating the best corrosion resistance of Mg-5Li alloy.

Regarding the corrosion process in depth, typical 3D CLSM images illustrates the effect of lithium content on the depth of corrosion pits after immersion in 0.1 M NaCl solution for different time (Fig. 10). Corrosion depth and width of Mg-1Li alloy are very sensitive to the immersion time, as shown in Fig. 10a-c. The shallow corrosion pits (177 μm) of Mg-1Li alloy after 4 h immersion turn into larger and a little deeper pits (222 μm) of 8 h immersion and then to much deeper corrosion grooves (391 μm) of 16 h immersion. For Mg-3Li and Mg-5Li alloys, the corrosion depth is not sensitive to the immersion time before 8 h and only the corroded width enlarges, whereas the corrosion depth of Mg-5Li alloy is always less than that of Mg-3Li alloy at the same immersion time. However, the corrosion depth of Mg-3Li alloy shows an dramatic increment from 172 μm of 8 h immersion to 390 μm of 16 h immersion, whilst the ascending value of corroded depth (from 148 μm, 8 h to 267 μm, 16 h) for Mg-5Li alloy is slow relatively. Based on the above analysis and description, the high lithium concentration in HCP Mg–Li alloys can suppress corrosion sensitivity to the immersion time in NaCl solution.

Additionally, electrochemical testing is also an rational and acceptant approach generally to evaluate the corrosion resistance and/or mechanisms of the materials. Herein, the potentiodynamic polarization and electrochemical impedance

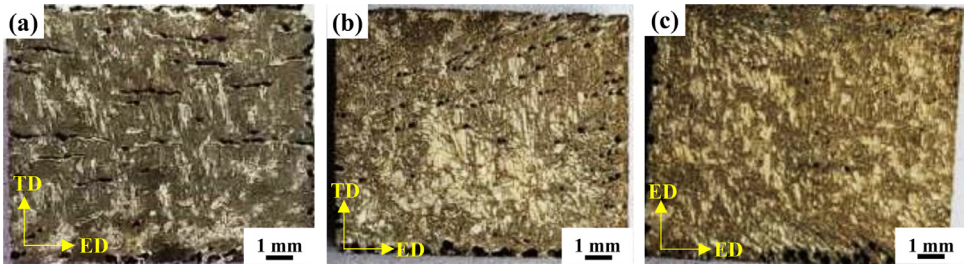

Fig. 8. Surface corrosion following the removal of corrosion products for (a) Mg-1Li, (b) Mg-3Li and (c) Mg-5Li alloys imposed to 0.1 M NaCl for 16 h.

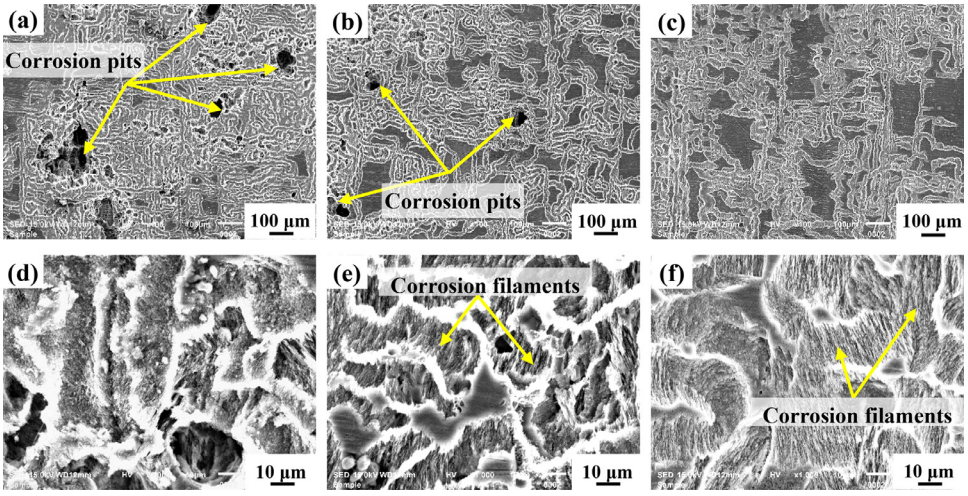

Fig. 9. SEM observations to specimen surfaces following the removal of corrosion products for (a) Mg-1Li, (b) Mg-3Li and (c) Mg-5Li exposed to 0.1 M NaCl for 2 h. Images (d), (e) and (f) are higher-magnification observations to the localization in images (a), (b) and (c), respectively.

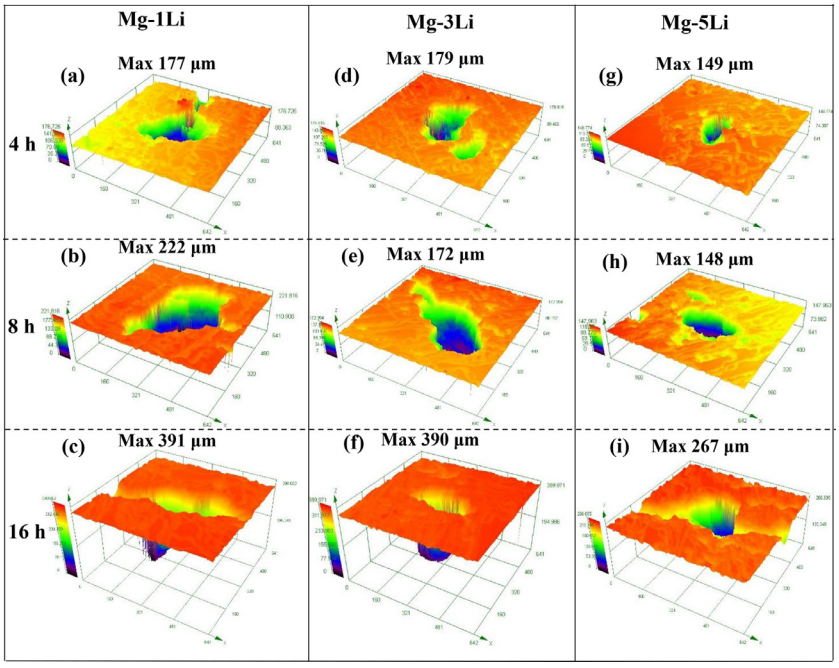

Fig. 10. Representative 3D CLSM images of (a-c) Mg-1Li, (d-f) Mg-3Li and (g-i) Mg-5Li alloys subjected to immersion in 0.1 M NaCl solution for (a) (d) (g) 4 h, (b) (e) (h) 8 h and (c) (f) (i) 16 h.

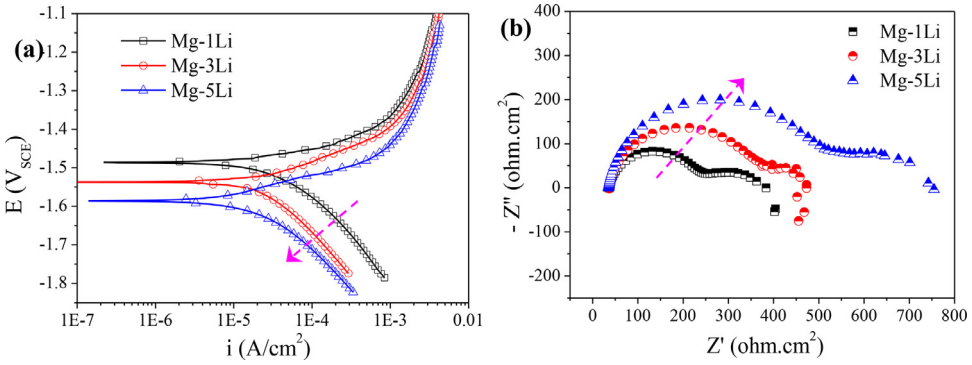

Fig. 11. (a) Potentiodynamic polarization curves and (b) EIS spectra (Nyquist plots) of Mg-1Li, Mg-3Li and Mg-5Li alloys measured in 0.1 M NaCl solution.

Table 3
Tafel fitting results derived from the polarization curves of the three Mg–Li alloys in 0.1 M NaCl.

Alloy	E_{corr} (V_{SCE})	i_{corr} (A/cm^2)
Mg-1Li	−1.49±0.02	(1.05±0.15) × 10^{-5}
Mg-3Li	−1.54±0.03	(8.03±0.21) × 10^{-6}
Mg-5Li	−1.59±0.02	(6.89±0.26) × 10^{-6}

spectroscopy (EIS) measurements are carried out to further elucidate electrochemical response of the three Mg–Li alloys, and the corresponding polarization curves and Nyquist plots are shown in Fig. 11. Based on the measured polarization response of the three Mg–Li (Fig. 11a), it is possible to speculate that the cathodic hydrogen evolution reaction (HER) kinetics decrease gradually with the increasing lithium content (denoted by the arrow). The anodic reaction kinetics of the studied Mg–Li alloys in 0.1 M NaCl implies a low anodic Tafel slope and no apparent passivation. Even though a visual shift in the polarization curves, it seems that the anodic Tafel slope associated with the anodic partial reaction is essentially unchanged with the alteration of lithium concentration, such that the controlling factor (in terms of corrosion current density) is where the cathodic kinetics intersect to form corrosion potential (E_{corr}). It is rationalized from the potentiodynamic polarization data that E_{corr} is increased with the descending lithium content. The detailed corrosion parameters are fitted by Tafel extrapolation and the results are listed in Table 3. The Mg-5Li alloy presents the lowest corrosion current density (i_{corr}) of 6.89 × 10^{-6} A/cm^2, whilst i_{corr} values of Mg-1Li and Mg-3Li alloys are about 1.05 × 10^{-5} A /cm^2 and 8.03 × 10^{-6} A/cm^2, respectively. Therefore, Mg-5Li alloy containing the highest lithium content exhibits the best corrosion resistance.

The Nyquist plots of the three Mg–Li alloys present the form characteristic of Mg alloys [56], whereby there is a high frequency capacitive loop, and an additional medium-to-low frequency capacitive loop that extends into the third quadrant with decreasing frequency (often termed an inductive loop) (Fig. 11b). The high frequency capacitance loops are attributed to the electric double layer at the interface between Mg substrate and 0.1 M NaCl electrolyte [37,43,57]. The medium frequency capacitance loops are related to the surface film [35]. Existence of low frequency inductive loop can be ascribed to the surface film with insufficiently protective function and corrosion nucleation at the initiation stage of localized corrosion. In addition, the capacitance loop dimension is enlarged obviously with the increasing lithium content in the three Mg–Li alloys. In general, the larger capacitance loop of Mg alloys indicate the lower dissolution rate, which also demonstrates that compact films are formed on the surface. As a result, the corrosion rate of the HCP Mg–Li alloys decreases and the film protection function enhances with the increasing lithium content.

4. Discussion

4.1. Effect of lithium content on the microstructure and mechanical behavior

As for the three HCP Mg–Li alloys studied in this work, the natural difference is the lithium content as their casting and processing technologies/parameters are always constant. On the other hand, the different lithium addition can result in different recrystallized microstructure and/or crystallographic texture during hot extrusion. In general, it is acceptant that non-basal slip of magnesium can be activated with the addition of lithium at room temperature [21–29]. In a previous study of Mg–Li single crystal deformation at room temperature and below, a strong evidence for the enhancement of $\langle c+a \rangle$ slip by lithium additions was found as the critical resolved shear stress (CRSS) of $\langle c+a \rangle$ slip was lower than that of prismatic $\langle a \rangle$ slip at low temperatures [26]. Herein, the texture and grain orientation characters of the as-extruded Mg-5Li alloy (Figs. 3 and 4) imply that large amounts of non-basal slips can be activated during the tension. In terms of the finer grains in Mg-5Li alloy, it can be possibly explained as following: more non-basal dislocations appear in the extrusion process, which turn into the potential nucleation sites in the following dynamic recrystallization (DRX) process and then promote grain refinement. DRX is a process involving nucleation and growth of new grains, which is influenced by many factors including deformation degree, deformation temperature, solute atoms and second phases. Because the extrusion temperature is same and no other third alloying element in the studied Mg–Li alloys, the change of their microstructure can

be attributed only to the lithium composition. Generally, the nucleation rate and growth rate of recrystallization decrease with the increase of alloying element content [23]. Moreover, it has been reported that recrystallization temperature of Mg–Li alloys increases with increasing Li content [23]. As a result, the DRX fraction of Mg-5Li alloy is the lowest in the studied HCP Mg–Li alloys. On the other hand, the refine grain size can further improve the mechanical performance of Mg-5Li alloy based on the Hall-Petch relationship [58].

Furthermore, the texture analysis indicates that as-extruded HCP Mg-*x*Li ($x = 1, 3, 5$) alloys present a texture element with basal planes rotated ~45° of Mg-1Li, ~80° of Mg-3Li and ~85° of Mg-5Li with respect to the extrusion direction (ED). A texture element of rotated basal planes of ~90° with respect to ED (*i.e.* the c-axis is approximately perpendicular to ED) was found in as-extruded Mg-4Li alloy with and without icosahedral phase [30]. On the other hand, the 45° basal texture of Mg-1Li alloy is altered into prismatic texture with the increasing lithium content in Mg-3Li and Mg-5Li alloys, concomitant with the similar results documented by previous works [21,29]. In the research of effect of Li content on the texture of Mg–Li alloys, Zeng et al. found that with the Li content increasing up to 2 wt%, the basal texture weakened by ~ 24% compared with the as-extruded Mg-1Li sheet, yet both of them showed a strong basal texture [21]. While in the as-extruded Mg-3Li sheet, the basal texture intensity dropped by ~ 80% and tilted towards the transverse direction (TD) by ~ 63°, and the prismatic pole figure showed a preferred orientation along the extrusion direction (ED) [21]. In this work, when the room temperature tensile test is conducted on the as-extruded Mg-1Li alloy, the c-axes of these grains will present about 45° with ED and TD tensile direction. At this point, the Schmid factor for the basal slip is maximum, and the non-basal slip is hardly to activate for its large CRSS at room temperature. Herein, Schmidt factor (SF) can be expressed as [30,59]: $SF = \cos\Phi\cos\lambda$, where Φ and λ (angles Φ and λ are complementary ($\Phi + \lambda = 90°$)) are the angles of tensile direction with respect to the normal direction of slip plane and optimal slip direction, respectively. Therefore, the mechanical anisotropy of Mg-1Li alloy along ED and TD is trivial due to the equivalent slip capacity along the basal planes presenting 45° with both ED and TD. With increasing lithium content, such as for Mg-3Li and Mg-5Li alloys, the c-axes of grains are inclined to tilt away ED and parallel to TD (Fig. 4), indicating a lower SF for the basal slip along ED and a reversed result for TD sample. Therefore, the apparent mechanical anisotropy with high strength and low ductility along ED occurs for Mg-3Li and Mg-5Li alloys.

4.2. Effect of lithium content on the corrosion behavior

In general, the refined grain size could improve the corrosion resistance of Mg in neutral NaCl electrolytes with little dissent [60,61]. The grain boundary can act as a physical corrosion barrier and the refined grain microstructure means much more grain boundaries in matrix, indicating a better corrosion resistance of small-grained microstructure than that of coarse-grained microstructure in magnesium [62]. As such, in this work, the refined grains are correlated with the high corrosion resistance of Mg-5Li alloy containing more lithium. Actually, the effect of crystallographic orientation on the corrosion of magnesium should also be considered herein. For magnesium alloys, one study examined Mg in 0.1 M NaCl and study grains after EBSD where near the {0001} planes were argued to be most corrosion resistant [63]. Recently, Bland and coauthors reported that the Mg {0001} surface exhibited corrosion susceptibility at the open circuit potential (OCP) while the {1010} and {1120} surfaces were passive at open circuit and pitting only initiated at potentials slightly anodic to their open circuit potentials in a similar environment [64]. As for the studied Mg-1Li alloy herein, its worst corrosion resistance should be correlated with the inclined 45° basal texture, as shown in Fig. 4. Based on the analysis of grain orientated distribution (Fig. 3), more and more {0110} and {1210} planes (the green and blue grains) are inclined to the normal direction when the lithium content is elevated in HCP Mg–Li alloys. Therefore, the grains with normal orientations along the {0110} and {1210} plane (the green and blue grains in Fig. 3) are difficult to be corroded in Mg-5Li alloy compared with 45° base (0001) plane in Mg-1Li alloy, leading to the high corrosion resistance of Mg-5Li alloy.

In fact, the variation in corrosion rate derived from thermomechanical processing effects, although a real effect, was not as large as the effect imparted by changes in alloying elements [65]. In this work, the surface film should play a key role in improving the binary HCP Mg–Li alloy with increasing lithium content, concomitant with the enlarged capacitive loops as shown in EIS plots (Fig. 11). In general, the composition of surface film on the traditional Mg alloys exposure to NaCl solution was porous $Mg(OH)_2$ combined with less MgO [66,67]. In terms of the Mg–Li alloys herein, the $Mg(OH)_2$ and MgO are inevitable in the surface film as that of traditional magnesium, whilst compounds containing lithium should also be existed due to its higher electrochemical/chemical activity. The XPS analysis of C 1 s on the Mg-*x*Li ($x = 1, 3, 5$, wt%) alloys after immersion in 0.1 M NaCl for 2 h are shown in Fig. 12. It can be seen that the peak corresponding Li_2CO_3 is enhanced with increasing lithium content. As a result, the effect of Li_2CO_3 on the surface film should be considered to elaborate the improving corrosion resistance of Mg-5Li alloy with more lithium content. Besides, the protective function of Li_2CO_3 film on BCC Mg–Li alloys was also reported recently [41-46]. Generally, the occurrence of degradation for Mg alloys could be attributed to:1) magnesium was an active metal and the passivation film composed of its oxide and hydroxide was only partially protective; 2) Cl^- adsorption was believed to be able to penetrate the surface film and destabilized the Mg atoms on the surface by weakening the bonding between the metallic atoms on the surface [34,68]. However, some attractive works could be referred recently to prove that high corrosion resistant Mg alloys were possibly classified to BCC Mg–Li systems due to the excellent Li_2CO_3 protective film deposited on the surface [41]. The underlaying mechanism on improving corrosion resistance of HCP Mg–Li

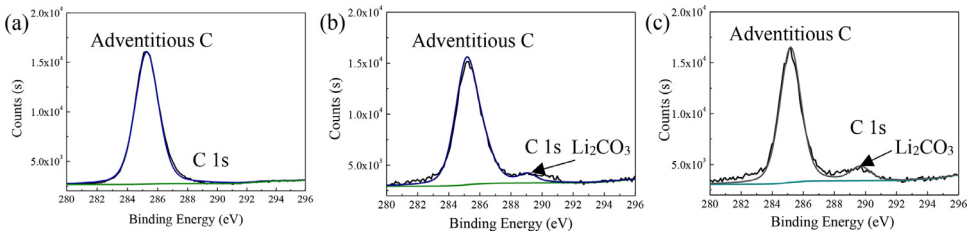

Fig. 12. XPS analysis of the surface film on Mg-1Li, Mg-3Li and Mg-5Li alloys after immersion in 0.1 M NaCl solution for 2 h.

alloy with increasing Li can be revealed as following: the high lithium concentration in Mg-5Li matrix accelerates the deposition of Li_2CO_3 compounds on the surface and the insoluble Li_2CO_3 compounds can further seal the porous $Mg(OH)_2$ to some extent, mitigating the permeation of aggressive Cl^- to destroy the surface film. Nevertheless, the protective film on the HCP Mg–Li alloys is not insistent like that on the BCC Mg–Li alloy, resulting in severe corrosion occurring in Mg-5Li alloy with a long term immersion (Fig. 10), similar results were reported in previous work [43].

5. Conclusions

Through investigating the effect of lithium content on the texture, mechanical and corrosion behaviours of HCP Mg-xLi (x = 1, 3, 5 wt%) alloys, the following conclusions can be drawn:

1 The increasing lithium content could reduce the dynamic recrystallization (DRX) of HCP Mg–Li alloys during hot extrusion and alter the 45° base (0001) texture of Mg-1Li alloy into prismatic texture of Mg-3Li and Mg-5Li alloys.
2 The 45° base (0001) texture causes the mechanical isotropy of Mg-1Li alloy, whilst the obvious mechanical anisotropy of Mg-3Li and Mg-5Li alloys are attributed to the strong prismatic (10–10) and (11–20) texture.
3 The groove-like corrosion of HCP Mg–Li alloys is weakened with increasing lithium content and the Mg-5Li alloys present the higher corrosion resistance, which is ascribed to the protective surface film, combined with the refined grains and the alteration of orientated prismatic (10–10) and (11–20) planes to the exposed surface in NaCl solution.

Declaration of Interest statement

None.

Acknowledgement

This work was supported financially by the National Natural Science Foundation of China (Grant No. 51901047), the Start-up Foundation of Guangdong University of Technology (No. 220413701) and National College Students Innovation and Entrepreneurship Training Program (Nos. 201911845185 and xj201911845345).

References

[1] R. Islam, M. Haghshenas, J. Magnes. Alloy. 7 (2019) 203–217.
[2] R. Wu, Y. Yan, G. Wang, L.E. Murr, W. Han, Z. Zhang, M. Zhang, Int. Mater. Rev. 60 (2015) 65–100.
[3] G. Liu, Z.D. Ma, G.B. Wei, T.C. Xu, X. Zhang, Y. Yang, W.D. Xie, X.D. Peng, J. Mater. Process. Tech. 267 (2019) 393–402.
[4] X.J. Wang, D.K. Xu, R.Z. Wu, X.B. Chen, Q.M. Peng, L. Jin, Y.C. Xing, Z.Q. Zhang, Y. Liu, X.H. Cheng, G. Chen, K.K. Deng, H.Y. Wang, J. Mater. Sci. Technol. 34 (2018) 245–247.
[5] T.M. Pollock, Science 328 (2010) 986–987.
[6] B.L. Mordike, T. Ebert, Mater. Sci. Eng. A 302 (2001) 37–45.
[7] A. Nayeb-Hashemi, J.B. Clark, Bulletin of Alloy Phase Diagrams 5 (1984) 365–374.
[8] M.V. Kral, B.C. Muddle, J.F. Nie, Mater. Sci. Eng. A 460-461 (2007) 227–232.
[9] Y. Jiang, Y.A. Chen, D. Fang, L. Jin, Mater. Sci. Eng. A 641 (2015) 256–262.
[10] Y. Zou, L.H. Zhang, Y. Li, H.T. Wang, J.B. Liu, P.K. Liaw, H.B. Bei, Z.W. Zhang, J. Alloys Compd. 735 (2018) 2625–2633.
[11] Z.L. Zhao, X.G. Xing, J.Y. Ma, L.P. Bian, W. Liang, Y.D. Wang, J. Mater. Sci. Technol. 34 (2018) 1564–1569.
[12] T. Mineta, H. Sato, Mater. Sci. Eng. A 735 (2018) 418–422.
[13] T. Al-Samman, Acta Mater. 57 (2009) 2229–2242.
[14] J.H. Zhang, S.J. Liu, R.Z. Wu, L.G. Hou, M.L. Zhang, J. Magnes. Alloy. 6 (2018) 277–291.
[15] Y. Tang, Q.C. Le, R.D.K. Misra, G.Q. Su, J.Z. Cui, Mater. Sci. Eng. A 712 (2018) 266–280.
[16] Y. Tang, Q.C. Le, W.T. Jia, X. Liu, J.Z. Cui, Mater. Sci. Eng. A 711 (2018) 1–11.
[17] F.R. Cao, J. Zhang, X. Ding, G.Q. Xue, S.Y. Liu, C.F. Sun, R.K. Su, X.M. Teng, Mater. Sci. Eng. A 760 (2019) 377–393.
[18] F. Zhong, H.J. Wu, Y.L. Jiao, R.Z. Wu, J.H. Zhang, L.G. Hou, M.L. Zhang, J. Mater. Sci. Technol. 39 (2020) 124–134.
[19] S.S. Park, B.S. You, D.J. Yoo, J. Mater. Process. Technol. 209 (2009) 5940–5943.
[20] D. Song, C. Li, N.N. Liang, F.L. Yang, J.H. Jiang, J.P. Sun, G.S. Wu, A.B. Ma, X.L. Ma, Mater. Des. 166 (2019) 107621.
[21] Y. Zeng, B. Jiang, Q.R. Yang, G.F. Quan, J.J. He, Z.T. Jiang, F.S. Pan, Mater. Sci. Eng. A 700 (2017) 59–65.
[22] H.T. Son, Y.H. Kim, D.W. Kim, J.H. Kim, H.S. Yu, J. Alloy. Compd. 564 (2013) 130–137.
[23] Y.H. Sun, R.C. Wang, J. Ren, C.Q. Peng, Z.Y. Cai, Mater. Sci. Eng. A 755 (2019) 201–210.
[24] E.W. Kelley, W.F. Hosford, Trans. Metall. Soc. AIME 242 (1968) 5–13.
[25] S.R. Agnew, M.H. Yoo, C.N. Tomé, Acta Mater 49 (2001) 4277–4289.
[26] S.R. Agnew, J.A. Horton, M.H. Yoo, Metall. Mater. Trans. A 33 (2002) 851–858.
[27] F. Guo, L. Liu, Y.L. Ma, L.Y. Jiang, Y.H. Zhang, D.F. Zhang, F.S. Pan, J. Alloy. Compd 813 (2020) 152117.
[28] Y. Zeng, B. Jiang, R.H. Li, J.J. He, X.S. Xia, F.S. Pan, Mater. Sci. Eng. A 631 (2015) 189–195.
[29] R.H. Li, F.S. Pan, B. Jiang, H.W. Dong, Q.S. Yang, Mater. Sci. Eng. A 562 (2013) 33–38.

[30] C.Q. Li, D.K. Xu, S. Yu, L.Y. Sheng, E.H. Han, J. Mater. Sci. Technol. 33 (2017) 475–480.
[31] D.K. Xu, C.Q. Li, B.J. Wang, E.H. Han, Mater. Des. 88 (2015) 88–97.
[32] C.Q. Li, D.K. Xu, B.J. Wang, L.Y. Sheng, R.Z. Wu, E.H. Han, J. Mater. Sci. Technol. 35 (2019) 2477–2484.
[33] B.J. Wang, J.Y. Luan, D.K. Xu, J. Sun, C.Q. Li, E.H. Han, Acta Metall. Sin-Eng. 32 (2019) 1–9.
[34] M. Esmaily, J.E. Svensson, S. Fajardo, N. Birbilis, G.S. Frankel, S. Virtanen, R. Arrabal, S. Thomas, L.G. Johansson, Prog. Mater. Sci. 89 (2017) 92–193.
[35] Y.W. Song, D.Y. Shan, R.S. Chen, E.H. Han, Corros. Sci. 51 (2009) 1087–1094.
[36] D.K. Xu, E.H. Han, Scr. Mater. 71 (2014) 21–24.
[37] Y.W. Song, D.Y. Shan, R.S. Chen, E.H. Han, J. Alloy. Compd 484 (2009) 585–590.
[38] T. Mineta, H. Sato, Mater. Sci. Eng. A 735 (2018) 418–422.
[39] R. Maurya, A.R. Siddiqui, K. Balani, Appl. Surf. Sci. 443 (2018) 429–440.
[40] P. Dinesh, S. Manivannan, S.P. Kumaresh Babu, S. Natarajan, Mater, Today: Proceed 15 (2019) 126–131.
[41] W.Q. Xu, N. Birbilis, G. Sha, Y. Wang, J. Daniels, Y. Xiao, M. Ferry, Nat. Mater. 14 (2015) 1229–1235.
[42] L.F. Hou, M. Raveggi, X.B. Chen, W.Q. Xu, K.J. Laws, Y.H. Wei, M. Ferry, N. Birbilis, J. Electrochem. Soc. 163 (2016) C324–C329.
[43] C.Q. Li, D.K. Xu, X.-.B. Chen, B.J. Wang, R.Z. Wu, E.H. Han, N. Birbilis, Electrochim. Acta 260 (2018) 55–64.
[44] Y.M. Yan, P. Zhou, O. Gharbi, Z.R. Zeng, X.B. Chen, P. Volovitch, K. Ogle, N. Birbilis, Electrochem. Commun. 99 (2019) 46–50.
[45] Y. Yan, Y. Qiu, O. Gharbi, N. Birbilis, P.N.H. Nakashima, App. Surf. Sci. 494 (2019) 1066–1071.
[46] Y.M. Yan, O. Gharbi, Maltseva A, X.B. Chen, Z.R. Zeng, S.W. Xu, W.Q. Xu, P. Volovich, M. Ferry, N. Birbilis, Corrosion 75 (2019) 80–89.
[47] C.Q. Li, D.K. Xu, Z.R. Zeng, B.J. Wang, L.Y. Sheng, X.B. Chen, E.H. Han, Mater. Des. 121 (2017) 430–441.
[48] R.L. Liu, J.R. Scully, G. Williams, N. Birbilis, Electrochim. Acta 260 (2018) 184–195.
[49] C.Q. Li, D.K. Xu, B.J. Wang, L.Y. Sheng, E.H. Han, J. Mater. Sci. Technol. 32 (2016) 1232–1238.
[50] C.Q. Li, D.K. Xu, T.T. Zu, E.H. Han, L. Wang, J. Magnes. Alloy. 3 (2015) 106–111.
[51] B.Q. Shi, L.Y. Zhao, D.C. Chen, C.Q. Li, Y. Dong, D. Wu, R.S. Chen, W. Ke, Mater. Sci. Eng. A 772 (2020) 138786.
[52] K.Sikdar Mahata, J. Magnes. Alloy. 4 (2016) 36–43.
[53] Z.P. Cano, M. Danaie, J.R. Kish, J.R. McDermid, G.A. Botton, G. Williams, Corrosion 71 (2015) 146–159.
[54] Z.P. Cano, J.R. McDermid, J.R. Kish, J. Electrochem. Soc. 162 (2015) 732–740.
[55] E. Ghali, W. Dietzel, K.U. Kainer, J. Mater. Eng. Perform. 13 (2004) 7–23.
[56] V. Shkirskiy, A.D. King, O. Gharbi, P. Volovitch, J.R. Scully, K. Ogle, N. Birbilis, Chem. Phys. Chem. 16 (2015) 536–539.
[57] G.L. Song, A. Atrens, D.H. StJohn, X.L. Wu, J. Nairn, Corros. Sci. 39 (1997) 1981–2004.
[58] H.H. Yu, Y.C. Xin, M.Y. Wang, Q. Liu, J. Mater. Sci. Technol. 34 (2018) 248–256.
[59] W.J. Ding, L. Jin, W.X. Wu, J. Dong, J. Nonferr. Met. 21 (2011) 2371–2381.
[60] K.D. Ralston, N. Birbilis, Corrosion 66 (2010) 075005–075005-13.
[61] N.N. Aung, W. Zhou, Corr. Sci. 52 (2010) 589–594.
[62] B. Jiang, Q. Xiang, A. Atrens, J.F. Song, F.S. Pan, Corr. Sci. 126 (2017) 374–380.
[63] M. Liu, D. Qiu, M.-.C. Zhao, G. Song, A. Atrens, Scr. Mater. 58 (2008) 421–424.
[64] L.G. Bland, K. Gusieva, J.R. Scully, Electrochim. Acta 227 (2017) 136–151.
[65] X. Xia, C.H.J. Davies, J.F. Nie, N. Birbilis, Corrosion 71 (2015) 38–49.
[66] M. Yeganeh, N. Mohammadi, J. Magnes. Alloy. 6 (2018) 59–70.
[67] M. Taheri, R.C. Phillips, J.R. Kish, G.A. Botton, Corros. Sci. 59 (2012) 222–228.
[68] Z. Luo, H. Zhun, T. Ying, D.J. Li, X.Q. Zeng, Surf. Sci. 672-673 (2018) 68–74.